Optode positional calibration in diffuse optical tomography

Jonathan J. Stott, Joseph P. Culver, Simon R. Arridge, and David A. Boas

Although diffuse optical tomography is a highly promising technique used to noninvasively image blood volume and oxygenation, the reconstructed data are sensitive to systemic differences between the forward model and the actual experimental conditions. In particular, small changes in optode location or in the optode–tissue coupling coefficient significantly degrade the quality of the reconstruction images. Accurate system calibration therefore is an essential part of any experimental protocol. We present a technique for simultaneously calibrating optode positions and reconstructing images that significantly improves image quality, as we demonstrate with simulations and phantom experiments. © 2003 Optical Society of America

OCIS codes: 170.5280, 170.6960.

1. Introduction

Diffuse optical tomography (DOT) is an emerging technique for noninvasive medical imaging.[1–3] By use of optical fibers, light is directed into biological tissue. As the light travels through the tissue it is scattered many times and exits as a diffuse photon fluence. The exiting photons are collected, and photodetectors record the intensity. Working in the diffusion approximation to the radiative transport equation,[4] the data can be interpreted to provide information about the optical scattering and absorption of the region probed by the photons.[5] If multiple overlapping measurements are available, tomographic reconstruction techniques can be used to produce three-dimensional images within the region of interest.[6] In addition, by operation at multiple wavelengths within the tissue, the optical absorption coefficients can be related back to the local concentration of oxyhemoglobin and deoxyhemoglobin (or, equivalently, to the total hemoglobin concentration and oxygen saturation). Knowledge of hemoglobin concentration has been used for functional imaging of human cerebral activity and as a tool to locate breast cancer based on the associated tumor vasculature.[1–3,7–11]

However, obtaining high-quality quantitative volume reconstructions of experimental data is one of the most difficult problems in DOT. The DOT inverse problem is ill-posed and generally underdetermined; therefore direct inversion of the data is not possible, and regularized pseudoinverse techniques must be used instead.[12] Furthermore, small mismatches between the forward model (and the approximations that necessarily go with it) and the actual experimental conditions can easily produce artifacts significantly larger than the signals of interest.

One way to compensate for systematic coupling errors is to use difference imaging.[7,13] Difference imaging reconstructs changes in the system relative to some reference measurement. In functional brain imaging, for example, the quantity of interest is changes in blood oxygenation as the subject performs some task, and these measurements can be directly compared with measurements taken while the subject is at rest.[7] These measurements do not depend on many potential sources of systematic error such as the amplitude coupling coefficients and, empirically at least, seem to be fairly robust against small optode (source and detector) positional errors.

Difference imaging, however, cannot be used when either absolute baseline optical properties are required (as opposed to absolute changes in the optical properties) or when only a single frame of data is

---

J. J. Stott (jstott@nmr.mgh.harvard.edu), D. A. Boas (dboas@nmr.mgh.harvard.edu), and J. P. Culver are with the Harvard Medical School—Massachusetts Institute of Technology Athinoula A. Martinos Center for Biomedical Imaging, Massachusetts General Hospital, 13th Street, Building 149, Charlestown, Massachusetts 02129. S. R. Arridge is with the Department of Computer Science, University College London, Gower Street, London WC1E 6BT, UK.

Received 7 October 2002; revised manuscript received 17 January 2003.

0003-6935/03/163154-09$15.00/0

available (i.e., there are not two sets of data to difference image). These are important limitations; knowledge of the local blood volume and oxygen saturation (which is computed from the absolute baseline optical properties) is important for stroke monitoring and in diagnostic breast imaging. Furthermore, for these applications, difference measurements are not generally available. For these imaging problems, therefore, accurate system calibration is essential to reduce systematic errors, otherwise the reconstructed image quality will be dominated by imaging artifacts larger than the desired signals. In a previous paper we developed an algorithm for finding the source and detector amplitude coupling coefficients from experimental data and showed that the coupling coefficients and three-dimensional images could be determined simultaneously.[14] In this paper we extend that technique to correct for both amplitude and positional errors while simultaneously imaging from a single frame of experimental data. This technique reduces model mismatch and leads to significant improvements in image quality.

2. Theory

A. Amplitude Calibration

Our algorithm for optode amplitude calibration was published previously.[14] Because of its conceptual similarity to positional calibration, however, we take the time here to briefly review the technique.

First, to every source $i = 1 \ldots N_s$, we assign an unknown scale factor $S_i(\lambda)$. This represents the uncalibrated laser power, fiber coupling losses, fiber attenuation, skin blemishes, superficial blood vessels, and any other source amplitude coupling terms. The scale factors will also vary with wavelength λ. Similarly, to every detector $j = 1 \ldots N_d$, we assign unknown scale factors $D_j(\lambda)$, which will also vary with wavelength. Each experimental measurement therefore consists of some ideal measurement value ϕ^{theory} multiplied by two unknown scale factors S and D:

$$\phi_i^{\text{meas}} = S_{j(i)}(\lambda_{l(i)}) D_{k(i)}(\lambda_{l(i)}) \phi_i^{\text{theory}}, \tag{1}$$

where $S_{j(i)}$ is the amplitude coefficient of the source j used to make measurement i, $D_{k(i)}$ is the detector coefficient of the detector k used to make measurement i, $\lambda_{l(i)}$ is the wavelength l at which the measurement was performed, and ϕ_i^{theory} is the ideal ($S = D = 1$) measurement. For homogeneous systems (e.g., tissue phantoms), ϕ_i^{theory} is also the quantity predicted by the forward model.[15–18] Taking the logarithm of both sides of Eq. (1), which is closely related to working in the Rytov approximation instead of the Born approximation, we solve for the unknown scale factors $\log[S_j(\lambda_l)]$ and $\log[D_k(\lambda_l)]$ in a least-squared sense by minimizing the difference between the predicted scaled measurements ϕ_i^{theory} and the experimental data ϕ_i^{meas}. This is equivalent to our minimizing the functional

$$F(\mathbf{S}, \mathbf{D}) = \sum_{1}^{N_m} \frac{1}{\sigma_i^2} |\log(\phi_i^{\text{meas}}/\phi_i^{\text{theory}}) - \log[S_{j(i)}] - \log[D_{k(i)}]|^2, \tag{2}$$

where N_m is the total number of measurements, σ_i^2 is the variance of each measurement, and the variation is with respect to the unknowns $\log S_j$ and $\log D_k$. The wavelength dependence of S_j and D_k in Eq. (2) was dropped for clarity. Coefficients S_j and D_k are then calculated from their respective logarithms.

The minimization of Eq. (2) with respect to $\log S_j$ and $\log D_k$ leads to a constant matrix $[\mathbf{J}_S|\mathbf{J}_D]$ that is rank deficient because the source and detector coefficients always occur as products; doubling all the source coefficients and halving the detector coefficients leaves the overall scale factors unchanged. It is therefore necessary to fix the value of any one coefficient at some arbitrary value (e.g., $D_1 = 1.0$ for all λ_l).[14] Although this sets the general amplitude scale of both the source and the detector terms, because they occur in pairs (source times detector), the overall amplitude scale is unconstrained and can take on whatever amplitude is needed to match the experimental data.

To make this more concrete, consider an idealized system where the correct scale factor for both sources and detectors is 10.0. The overall amplitude factor seen at the imager is therefore 100.0 (sources times detectors). If we fix one of the sources at 1.0, this will set the scale of all the source coefficients to be 1.0. The detector coefficients, however, remain unconstrained and will take a value of 100.0 to maintain the overall amplitude scale. Thus, although neither the sources nor the detectors have their correct value, their product (which is the one quantity of interest to us) does have the correct value of 100.0.

When the number of measurements N_m is much greater than the number of coupling coefficients (the number of sources plus the number of detectors), amplitude calibration leads to significantly improved image quality.[14]

B. Positional Calibration

We now extend the technique of Subsection 2.A to the correction of positional errors. Given an appropriate forward model,[15–19] we can compute the incident fluence

$$\phi_i^{\text{theory}} = \phi^{\text{theory}}[\mathbf{r}_{s,j(i)}, \mathbf{r}_{d,k(i)}],$$

where $\mathbf{r}_{s,j(i)}$ is the nominal position of the source j used to make the ith measurement and $\mathbf{r}_{d,k(i)}$ is the nominal position of the detector k used to make the ith measurement. The actual optode positions can be displaced from their nominal positions by some set of vector offsets $\Delta\mathbf{r}$. This displacement leads to a mismatch between the forward model used to compute the fluence and the measured incident fluence that, if left uncorrected, will distort the image reconstruction. To calibrate the optode positions, we iteratively update the position vector used by the forward model so as to minimize the weighted mean-square difference between the predicted and the measured fluences. This is equivalent to our minimizing the functional F:

$$F(\mathbf{S}, \mathbf{D}, \mathbf{r}_s, \mathbf{r}_d) = \sum_{i=1}^{N_m} \frac{1}{\sigma_i^2} |\log(\phi_i^{\text{meas}}/\phi_i^{\text{theory}}) - \log[S_{j(i)}] - \log[D_{k(i)}]|^2, \tag{3}$$

where the ϕ_i^{theory} are explicit functions of the position vectors $\mathbf{r}_s$ and $\mathbf{r}_d$. In contrast to Eq. (2), Eq. (3) is nonlinear in the $\mathbf{r}_s$ and the $\mathbf{r}_d$, and so an appropriate nonlinear optimization scheme must be employed. This approach is easily extended to allow one to simultaneously update the amplitude coefficients, the positional correction, and the variation in the optical properties of the medium.

For simplicity, we first consider just positional error minimization. Let the minimum of Eq. (3) be at some set of positions $\mathbf{R}_j = \mathbf{r}_j + \Delta\mathbf{r}_j$ where $\mathbf{R}_j$ can be a component of either the source or the detector position vector as needed and $\Delta\mathbf{r}_j$ is initially unknown. If we could solve for the $\Delta\mathbf{r}_j$ directly, we could jump directly to the minimum in a single iteration. For nonlinear equations, unfortunately, this is not generally possible, and we have to content ourselves with a local estimate of the $\Delta\mathbf{r}_i$ that will serve as our update step for this iteration.

Linearizing Eq. (3) (and ignoring the S and D terms) leads to the update vector

$$\Delta\mathbf{r} = -\left(\frac{1}{\sigma^2} \mathbf{J}_R^T \mathbf{J}_R\right)^{-1} \mathbf{J}_R^T \mathbf{y}, \tag{4}$$

where the elements of the Jacobian matrix $\mathbf{J}_R$ are given by

$$J_{i,n} = \frac{\partial}{\partial \mathbf{r}_n} \log \phi_i^{\text{theory}},$$

where $\mathbf{r}_n$ is the nth element of the update vector

$$\mathbf{r} = (\mathbf{r}_{s,1}, \mathbf{r}_{s,2}, \ldots, \mathbf{r}_{s,n_s}, \mathbf{r}_{d,1}, \mathbf{r}_{d,2}, \ldots, \mathbf{r}_{d,n_d}),$$

and the elements of the column vector $\mathbf{y}$ are given by

$$y_i = \log(\phi_i^{\text{meas}}/\phi_i^{\text{theory}}).$$

As before, the ϕ_i^{theory} are explicit functions of the vectors $\mathbf{r}_s$ and $\mathbf{r}_d$. If an analytical expression for ϕ^{theory} is available then the Jacobian can be calculated analytically, otherwise the derivatives needed to generate $\mathbf{J}_R$ can be computed numerically by a finite-difference approximation for the derivative. To keep our computer code as general as possible, we computed all the derivatives used in this paper numerically using Euler's method.[20] Euler's method requires two function evaluations to compute the derivative. Thus an upper bound on the computational effort is $2N_J$ function evaluations where N_J is the number of matrix elements in $\mathbf{J}$. If more than one derivative is taken at the same point, however, then one of the two function evaluations can be recycled from the previous calculation. Thus the actual computational effort required will usually be somewhat less.

Because the inverse in Eq. (4) can be singular, especially near a minima where the derivatives go to zero, it is generally necessary to compute the regularized inverse of $\mathbf{J}_R^T\mathbf{J}_R$ when one is updating the position vector $\Delta\mathbf{r}$ instead of the true matrix inverse:

$$(\mathbf{J}_R^T\mathbf{J}_R)^{-1} \approx (\mathbf{J}_R^T\mathbf{J}_R + \alpha\mathbf{I})^{-1}\mathbf{J}_R^T,$$

where $\mathbf{I}$ is the identity matrix and α is the regularization parameter; $0 \leq \alpha < \infty$. At each iteration, the Jacobian $\mathbf{J}_R$ is computed by use of the current optode positions. The update $\Delta\mathbf{r}$ is then computed with Eq. (4), and the position of each optode is updated: $\mathbf{r}_{i+1} = \mathbf{r}_i + \Delta\mathbf{r}_i$. The process repeats until the optode positions have sufficiently converged.

C. Calibrated Reconstructions

In the full inverse problem we would consider the minimization of a functional

$$F(\mu_a, \mu_s', \mathbf{S}, \mathbf{D}, \mathbf{r}_s, \mathbf{r}_d) = \sum_{1}^{N_m} \frac{1}{\sigma_i^2} |\log(\phi_i^{\text{meas}}/\phi_i^{\text{theory}}) - \log[S_{j(i)}] - \log[D_{k(i)}]|^2, \tag{5}$$

where ϕ_i^{theory} is now also a function of μ_a and μ_s':

$$\phi_i^{\text{theory}} = \phi_i^{\text{theory}}[\mathbf{r}_{s,j(i)}, \mathbf{r}_{d,k(i)}; \mu_a; \mu_s'].$$

Linearization leads to the set of equations

$$\mathbf{y} = [\mathbf{J}_{\mu_a}|\mathbf{J}_{\mu_s'}|\mathbf{J}_S|\mathbf{J}_D|\mathbf{J}_R]\Delta\mathbf{x}, \tag{6}$$

where $\Delta\mathbf{x} = [\Delta\mu_a, \Delta\mu_s', \Delta \log \mathbf{S}, \Delta \log \mathbf{D}, \Delta\mathbf{r}_s, \Delta\mathbf{r}_d]$ and the matrices $\mathbf{J}_{\mu_a}$ and $\mathbf{J}_{\mu_s}'$ are the Jacobian matrices for variations in the optical properties μ_a and μ_s', as described in previous publications.[21] Equation (6) can be solved for $\Delta\mathbf{x}$ by iterative methods as shown above, which updates all five of the Jacobian terms $\mathbf{J}_{\mu_a}$, $\mathbf{J}_{\mu_s}'$, $\mathbf{J}_S$, $\mathbf{J}_D$, and $\mathbf{J}_R$ after each iteration. Note that the mixture of physical dimensions in the different $\mathbf{J}$ can lead to numerical stability issues that change with choice of units, so it is useful to rescale the matrices to dimensionless quantities.[14]

3. Results

A. Simulation

To demonstrate the improvements in image reconstruction quality, we applied positional calibration to both simulated and experimental data. For the simulated data, we modeled a homogeneous medium using the analytical slab solution of the diffusion equation as our forward model.[16]

For our first simulation, we used a 3 by 3 array of sources and a 3 by 3 array of detectors located on the opposite surface of a 6-cm slab. The optical properties used were $\mu_s' = 10\ \text{cm}^{-1}$ and $\mu_a = 0.10\ \text{cm}^{-1}$ as

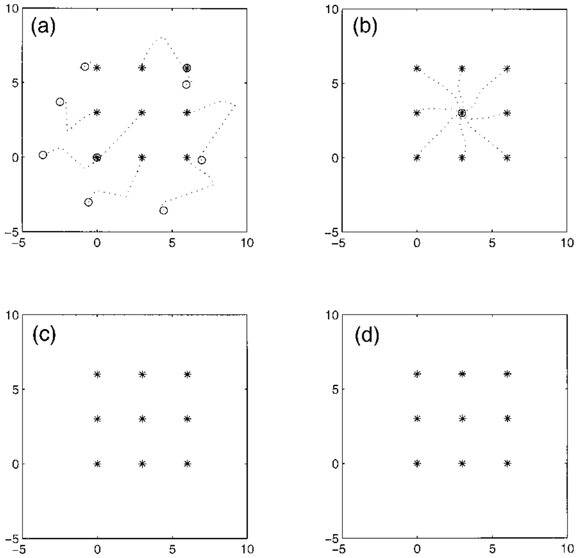

Fig. 1. Trajectories of the individual optode positions during calibration. (a) and (b) show the source and detector trajectories, respectively, where the starting positions are marked by the circles and the final positions are marked by stars. (c) and (d) show the actual optode source and detector positions, respectively.

were the accurately known source and detector amplitude coefficients. As an initial guess, we displaced the source positions randomly from their correct positions with a standard deviation of 2.0 cm and placed all nine detectors at the center of the actual detector array. Figure 1 shows the trajectories of the individual sources and detectors as the algorithm iteratively corrects positional errors. With calibration, the average positional error was reduced from 2.8 to just 0.0032 cm. To improve visual clarity of the traces, we did not take the full update step each iteration; instead we used

$$\mathbf{r}_{n+1} = 0.4\boldsymbol{\Delta}\mathbf{r} + \mathbf{r}_n,$$

where $\mathbf{r}_n$ is the estimate of the positional correction after n iterations and $\boldsymbol{\Delta}\mathbf{r}$ is the update computed from Eq. (4). These results appear to be robust; in the absence of noise, we obtained convergence to the correct source and detector locations for every set of random initial guess we tried.

Note that, because of the translational and rotational symmetry intrinsic to the slab geometry we used, we needed to fix two optodes at their correct location. When these two locations are not fixed, the positions converge to the correct relative orientation but with a random translational and rotational offset (because of the translational and rotational invariance of the forward model). Fixing only one optode at its correct location breaks the translational symmetry but not the rotational symmetry. Fixing either of the two optodes at an incorrect location naturally distorts the entire layout. This step is necessary only with homogeneous data (simulated or experimental); heterogeneities within the medium break the symmetry. Fixing the location of one optode, however, does seem to improve the convergence slightly even in the case of heterogeneous media.

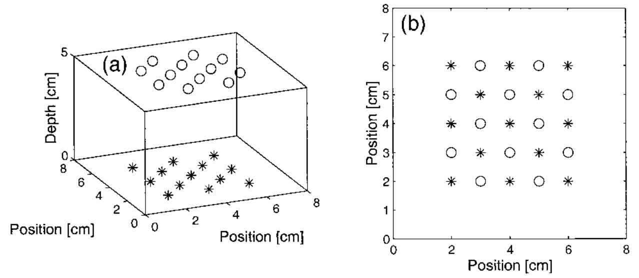

Fig. 2. Two views of the source–detector geometry used to generate our simulation results. (a) Simulation geometry; (b) geometry top view. Sources (stars) are in the $Z = 0$ plane; detectors (circles) are in the $Z = 5$-cm plane.

For our second simulation, we modeled a more realistic imaging problem. For optical properties, we used $\mu_s{}' = 8\ \text{cm}^{-1}$ and $\mu_a = 0.05\ \text{cm}^{-1}$. The source–detector geometry we used is shown in Fig. 2. We used a total of 13 sources alternating with 12 detectors, each on a square lattice. The sources define the $Z = 0$ plane, and the detectors were at $Z = 5$ cm. We reconstructed a volume 8 cm × 8 cm × 5 divided into voxels 0.5 cm on a side. We perturbed the source and detector amplitude coefficients randomly with a standard deviation of 10% about their nominal value of 1.0. We displaced the source and detector positions a random distance in the X,Y plane where the displacements along both X and Y axes were Gaussian random numbers with standard deviations of 1 mm. Finally, we added a spherical perturbation with radius of 0.9 cm and an absorption 50% above background ($\mu_a{}^{\text{sphere}} = 0.075\ \text{cm}^{-1}$) to the imaging volume. Forward data were computed for the displaced positions, and −30 dB of Gaussian random noise was added to the simulated data [i.e., a signal-to-noise ratio (SNR) of approximately 1000:1].

The SNR was calculated relative to the total fluence (the experimentally accessible parameter). A typical perturbation in DOT introduces changes of the order of 1% of the incident field (a signal level of approximately −20 dB), so a 30-dB SNR relative to the total fluence is closer to a 10-dB SNR relative to the perturbation, and it is the perturbation that matters for imaging. Thus a 30-dB SNR is a reasonable choice for our simulation.

For reconstruction, we used the nominal source and detector amplitudes and positions as the initial guess. Because we were modeling a cw detector (amplitude data only), we reconstructed only the absorption perturbations. We performed all reconstructions using the Rytov approximation[6,22] and the linear reconstruction approach described in Subsection 2.B. The regularization parameter $\alpha = 10^{-3}$ $\max[\text{diag}(\mathbf{J}_R{}^T\mathbf{J}_R)]$ (chosen by trial and error to give good results) was used for all the reconstructions of this data set. The scale factor $\max[\text{diag}(\mathbf{J}_R{}^T\mathbf{J}_R)]$ was computed before the first iteration and was not

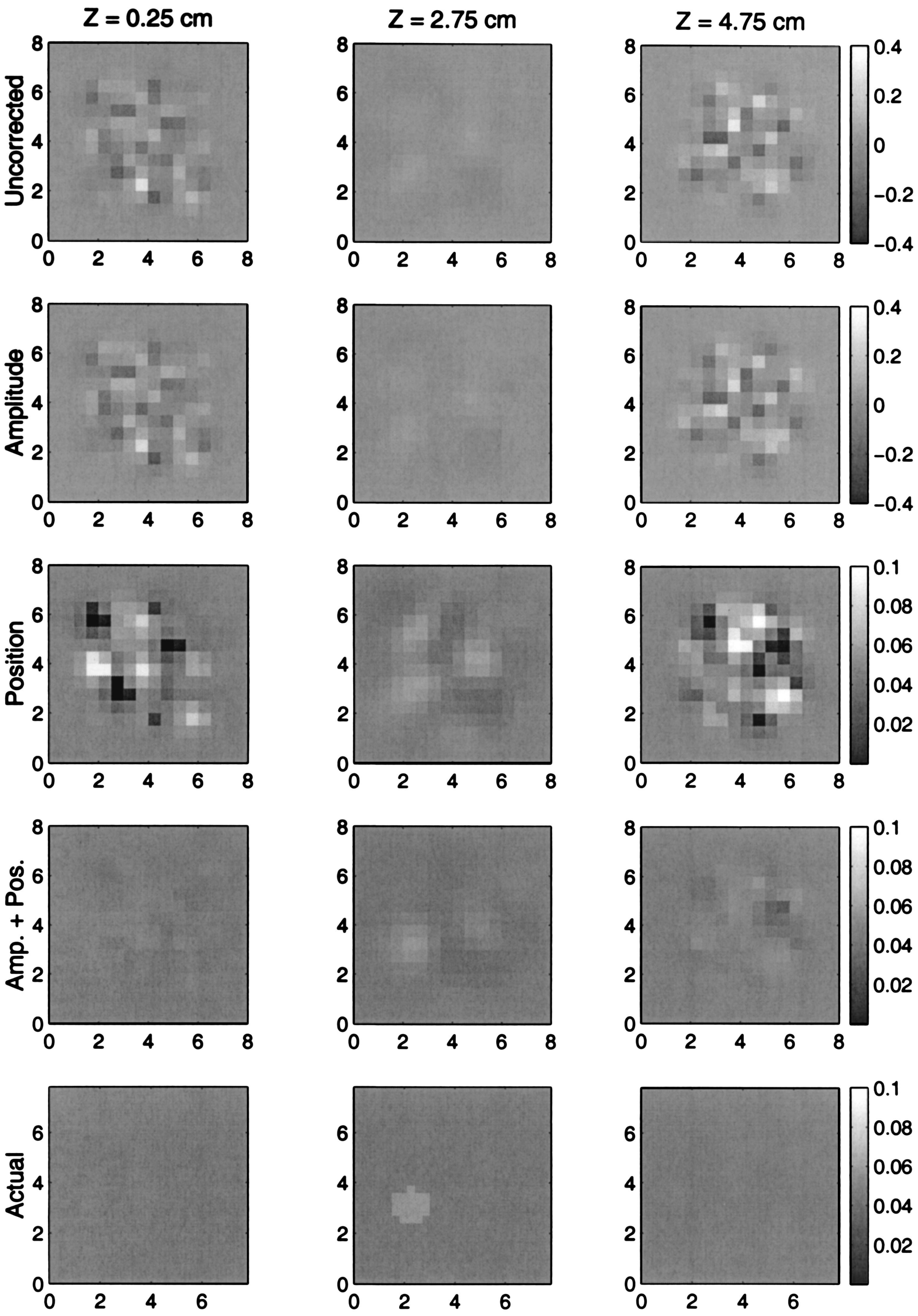

Fig. 3. Reconstructions of simulated data, with and without calibration. Each column is the reconstruction at a fixed depth (from left to right: $Z = 0.25$ cm, $Z = 2.75$ cm, and $Z = 4.75$ cm). The top row is a reconstruction of the data with no attempt made to correct for amplitude or positional errors. The second row was corrected for amplitude errors only; the third row was corrected for positional errors only. The fourth row was simultaneously corrected for both positional and amplitude errors. The bottom row is the actual inhomogeneity. Note the difference in scales between the top and bottom images.

changed thereafter. The algorithm was iterated until

$$\frac{|\epsilon_{n-1}| - |\epsilon_n|}{|\epsilon_{n-1}|} < 0.01,$$

at which point the algorithm was deemed to have converged. Here $|\epsilon_n|$ is the norm of the residual at the nth iteration.

Figure 3 shows reconstructed images for four different reconstruction schemes. Each column is a slice through the reconstruction at a different depth

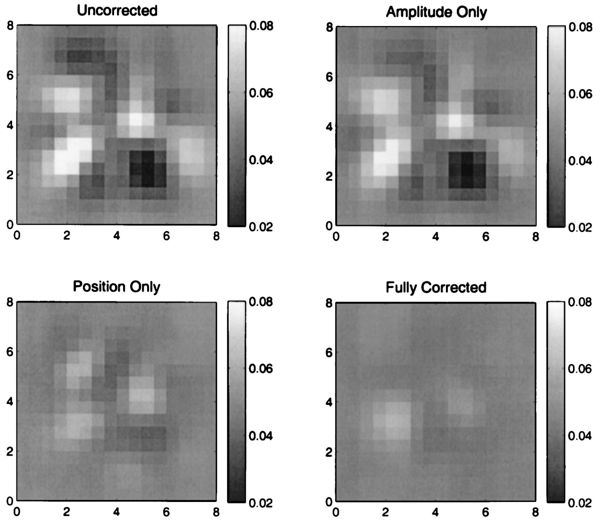

Fig. 4. Data from the middle ($Z = 2.75$ cm) column of Fig. 3, plotted with uniform gray scales. The correct background absorption is $\mu_a = 0.050\ \text{cm}^{-1}$, and the absorption inside the sphere is $\mu_a^{\text{sphere}} = 0.075\ \text{cm}^{-1}$. Even in the middle of the volume, positional calibration improves the reconstructed data.

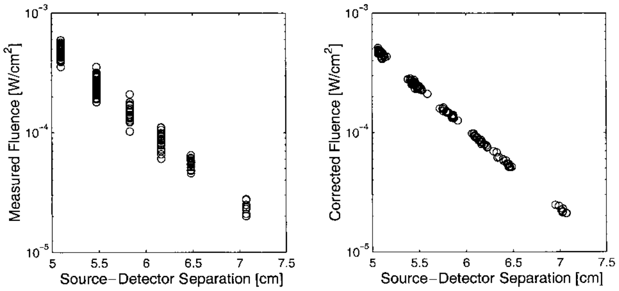

Fig. 5. Plots of detected fluence as a function of source–detector separation. (a) Simulated data plotted at the nominal source–detector positions. (b) The same data plotted at the source–detector positions after amplitude and positional error correction. For perfectly calibrated data, the points would sit on a single straight line.

(from left to right: $Z = 0.25$ cm, $Z = 2.75$ cm, and $Z = 4.75$ cm). The top row shows a direct linear reconstruction of the data. No attempt was made to correct for amplitude or positional errors. As might be expected given the large amplitude and positional errors, the image quality is quite poor especially near the optodes. The second row shows a linear reconstruction of the image with only amplitude correction. The image quality is slightly better than the uncorrected image, but the image is still dominated by reconstruction artifacts. The third row is the image reconstruction with only positional correction. The artifacts are much smaller (note the reduced scale), but they are still as large or larger than the actual signal. We reconstructed the fourth row using simultaneous amplitude and positional correction. The artifacts in the optode planes were largely eliminated, and the inhomogeneity is clearly visible in the middle frame. The final row is the original inhomogeneity. Figure 4 shows the same data as the middle ($Z = 2.75$ cm) column of Fig. 3, but is plotted with a uniform gray scale. This shows that the noise reduction that is due to positional calibration is significant not only in the plane of the optodes, but also in the center of the volume.

Figure 5 is a plot of the measured fluence as a function of source–detector separation for the simulation described above. If we had noise-free measurements at the correct source–detector separations and a homogeneous medium, the data would fall exponentially with increasing separation. When we use the nominal detector positions to compute the separations [Fig. 5(a)], the amplitude-corrected data show considerable variation in intensity at a given separation. When we use the corrected optode positions with amplitude correction [Fig. 5(b)], although there is still noise in the measurements, the graph is much closer to the ideal straight-line solution. Some of the remaining variation can also be attributed to the presence of the spherical inhomogeneity.

B. Experiment

To demonstrate our procedure using actual experimental data, we first inverted a set of homogeneous data collected on a phantom using our cw breast imager. For our breast imager, the fiber ends are attached to one of two fiber plates (one for sources, one for detectors). The fiber plates are designed to be inserted into a modified set of mammography compression plates (see Fig. 6). After the optical data are collected, the fiber plates are removed, and a digital x-ray image is taken without moving the patient. This x ray can be used later to provide coregistered structural information to supplement the optical data. As part of our clinical protocol, a set of standardized phantom measurements is made for every patient as a measure of image performance and to aid in data calibration. The first experimental data set that we reconstruct below (see Fig. 8) is one of

Fig. 6. Compression plates with fibers of our clinical breast imaging system. The plastic plates are standard mammography plates modified to hold our optical fiber arrays. The sources are on the bottom plate and fill roughly the middle third of the plate (only the ends of the fibers are clearly visible). Detector fibers can be seen coming out of the top plate. The imager electronics are to the right, outside the photo.

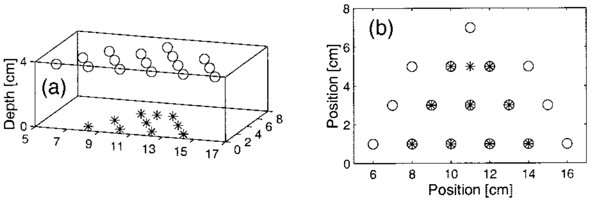

Fig. 7. Geometry of our clinical breast imaging system. (a) Simulation geometry, (b) geometry, top view. Sources (stars) are in the $Z = 0$ plane; detectors (circles) are located above. The thickness of the phantom was 3.7 cm.

these homogeneous phantom measurements. To simplify the interpretation of our results, however, data from only the 690-nm lasers were used in this paper.

The cw breast imager has 16 avalanche photodiode detectors and 18 LED sources, nine at 690 nm and nine at 830 nm. The sources are modulated at audio frequencies (4–8 kHz), and, because of all the individual sources, the signal at each detector is demodulated during postprocessing to yield the signal at each detector.

The source–detector geometry of our imager is shown in Fig. 7. The target was a homogeneous Intralipid tissue phantom with the nominal optical properties $\mu_s' = 10\ \mathrm{cm}^{-1}$ and $\mu_a = 0.044\ \mathrm{cm}^{-1}$. The thickness of the phantom was 3.7 cm, equal to that of the patient imaged just prior to collection of the phantom data. Although the fibers are fixed in metal plates, the gluing of the fibers produces small optode displacements. Also, angular deviations from normal incidence are almost indistinguishable from horizontal displacements when the line sources are replaced by point sources inside the tissue volume in the forward model. Finally, the patient and phantom thicknesses are known only to ± 1 mm.

Figure 8 shows our reconstructed images of the first set of phantom data. As before, each column is a slice through the volume at a fixed depth. The top row is a reconstruction from uncorrected data. The second row was corrected for positional but not amplitude errors. The third row was iteratively corrected for amplitude errors but not positional errors (which are clearly visible in both the source and the detector planes). The fourth row was iteratively corrected for both amplitude and positional errors, and the reconstructed images are significantly more uniform than the uncorrected or partially corrected im-

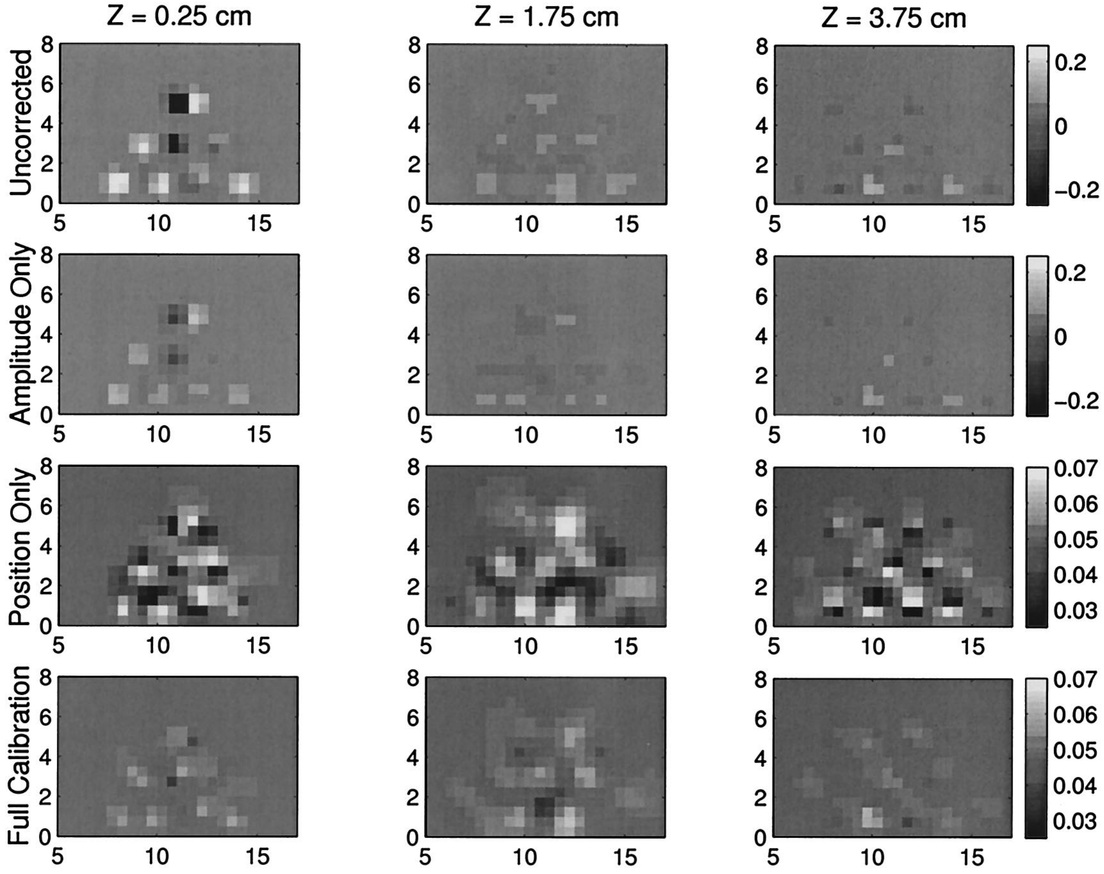

Fig. 8. Reconstructions of clinical phantom data, with and without error corrections. Each column is the reconstruction at a fixed depth (from left to right: $Z = 0.25$ cm, $Z = 1.75$ cm, and $Z = 3.75$ cm). The top row is a reconstruction of the data with no attempt made to correct for amplitude or positional errors. The second row was corrected for amplitude errors only; the third row was corrected for positional errors only. The fourth row was simultaneously corrected for both positional and amplitude errors. Note the difference in scales between the different rows.

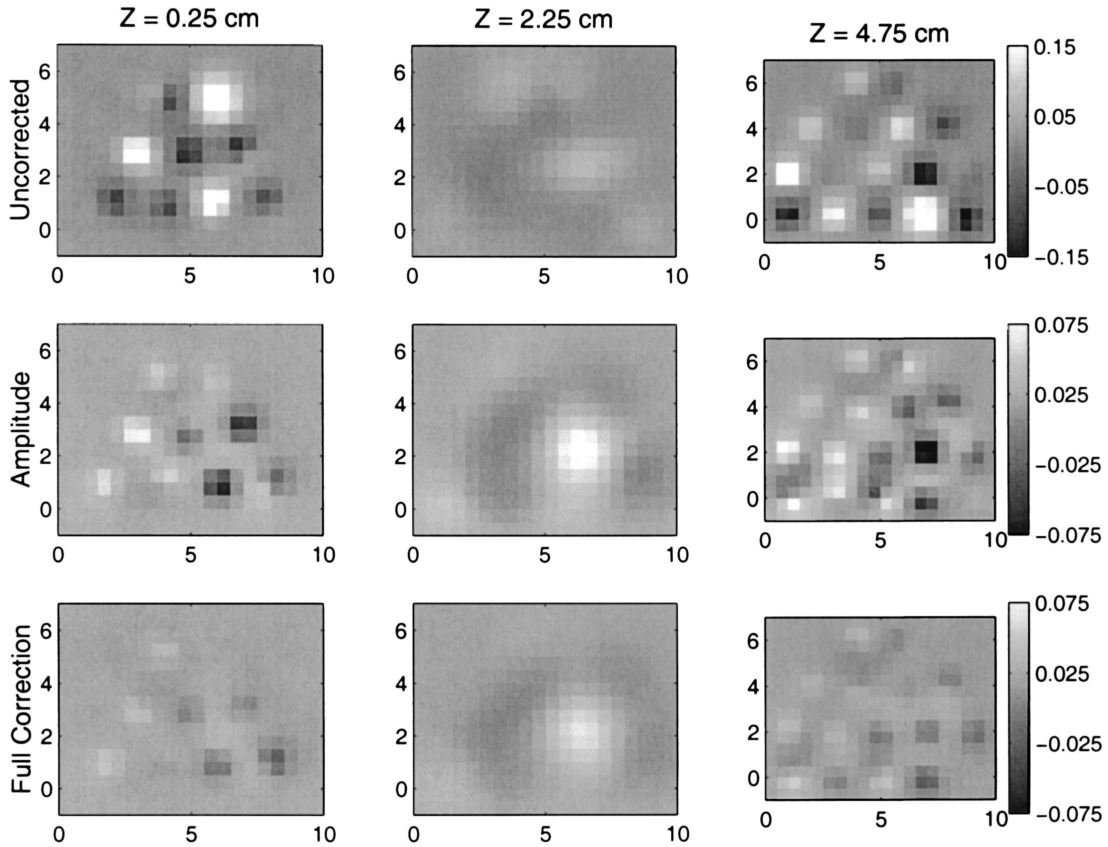

Fig. 9. Reconstructions of inhomogeneous laboratory phantom data, with and without error corrections. The inhomogeneity was a fluid-filled 2-cm glass sphere centered at approximately $x = 8.25$ cm, $y = 9.75$ cm, and $z = 4.75$ cm. Each column is a slice through the reconstruction at a fixed depth (from left to right: $Z = 0.25$ cm, $Z = 2.25$ cm, and $Z = 4.75$ cm). The top row is a reconstruction of the data with no attempt made to correct for amplitude or positional errors. The middle row was corrected for amplitude errors only. Artifacts in the source amplitude ($Z = 0$ plane) were greatly reduced, but the errors in the detectors ($Z = 5$ plane) remain. The bottom row was simultaneously corrected for both positional and amplitude errors. The artifacts in the source plane and the detector plane are significantly reduced, leaving a much cleaner reconstruction of the perturbation.

ages. We performed all reconstructions in the Rytov approximation using the linear reconstruction approach described in Subsection 2.B. The regularization parameter $\alpha = 10^{-2}\max[\mathrm{diag}(\mathbf{J}_R{}^T\mathbf{J}_R)]$ (chosen by trial and error to give good performance) was used for all reconstructions in Fig. 8. The scale factor $\max[\mathrm{diag}(\mathbf{J}_R{}^T\mathbf{J}_R)]$ was computed before the first iteration and was not changed thereafter. As with the simulated data, the algorithm was iterated until

$$\frac{|\epsilon_{n-1}| - |\epsilon_n|}{|\epsilon_{n-1}|} < 0.01,$$

at which point the algorithm was deemed to have converged.

As can be seen with the simulated data, the artifacts in the optode planes are particularly reduced by simultaneous amplitude and positional calibration. Because the phantom is homogeneous, a perfect reconstruction would be a uniform volume with a constant absorption coefficient. Although not as dramatic as the simulated data, probably because of the lower SNR, the corrected images nevertheless have significantly less noise than the uncorrected data.

Finally, to demonstrate that our algorithm works with nonuniform experimental systems data, we reconstructed a second set of experimental data. In this case, we imaged a 2-cm glass sphere into the middle of an Intralipid phantom. By pumping fluid with different optical properties (relative to the Intralipid background) through the sphere, we could reproduce a variety of experimental conditions. For this particular data set, the background optical properties were $\mu_s' = 8.0$ cm and $\mu_a = 0.019$ cm, and the sphere contained a mixture of pigs blood and Intralipid with approximately the same scattering but greater absorption than the background.

Figure 9 shows reconstructions of the second phantom. The geometry for this phantom is a mirror image of the previous phantom (Fig. 7). The thickness of the phantom was 5.1 cm. As before, the top row of Fig. 9 is the reconstruction with uncorrected data. The middle row is a reconstruction with only amplitude calibration. The artifacts in the source plane ($Z = 0$) and detector planes have been significantly reduced, which suggests that our amplitudes were especially uneven. The bottom row is a reconstruction with both amplitude and positional calibration and shows even better (but still not perfect) artifact reduction in both the source and the detector planes. The regularization parameter $\alpha = 1 \times 10^{-2} \max[\mathrm{diag}(\mathbf{J}_R{}^T\mathbf{J}_R)]$ (chosen by trial and error to give good performance) was used for all the reconstructions in Fig. 9. The scale factor $\max[\mathrm{diag}(\mathbf{J}_R{}^T\mathbf{J}_R)]$ was computed before the first iteration and was not changed thereafter. These results are typical; similar results were obtained for the other data sets (with different optical properties) that we collected as part of this experiment.

4. Conclusion

Although we derived the general theory in this paper, the extension of this technique to include certain types of constraint is also straightforward. For example, if no offset in the Z direction is possible (i.e., the displacements are constrained to lay in the X, Y plane), then the rows that represent displacements in Z can be deleted from the Jacobian. Uniform tilts, rotations, and translations can also be implemented by the addition of derivatives with respect to the relevant global parameters to the Jacobian.

In conclusion, positional correction is an important technique used to improve the accuracy of DOT data inversions. For a given set of experimental data and an appropriate forward model, positional correction adjusts the location of the source and detector fibers to minimize the mismatch between the model and the experimental data. When we iteratively update the positional correction, the amplitude correction, and the optical perturbations $\mu_s{}'$ and μ_a, significantly improved volume reconstructions are obtained.

The authors acknowledge the help of Tina Chaves and Quan Zhang in collecting the experimental phantom data. J. J. Stott also acknowledges Alex Barrett for a helpful discussion on high-dimensional optimization problems. This research was funded with support from Advanced Research Technologies, National Institutes of Health grant R01-CA97305, and from the Center for Minimally Invasive Therapies. S. R. Arridge also acknowledges the Wellcome Trust for a Biomedical Research Collaboration grant.

References

1. D. Grosenick, H. Wabnitz, H. H. Rinneberg, K. T. Moesta, and P. M. Schlag, "Development of a time-domain optical mammograph and first *in vivo* applications," Appl. Opt. **38,** 2927–2943 (1999).
2. S. Fantini, M. A. Franceschini, E. Gratton, D. Hueber, W. Rosenfeld, D. Maulik, P. G. Stubblefield, and M. R. Stankovic, "Non-invasive optical mapping of the piglet brain in real time," Opt. Exp. **4,** 308–314 (1999); http://www.opticsexpress.org.
3. T. O. McBride, B. W. Pogue, E. D. Gerety, S. B. Poplack, U. L. Osterberg, and K. D. Paulse, "Spectroscopic diffuse optical tomography for the quantitative assessment of hemoglobin concentration and oxygen saturation in breast tissue," Appl. Opt. **38,** 5480–5490 (1999).
4. S. Chandrasekhar, *Radiative Transfer* (Dover, New York, 1960).
5. A. Yodh and B. Chance, "Spectroscopy and imaging with diffusing light," Phys. Today **48,** 34–40 (1995).
6. A. C. Kak and M. Slaney, *Principles of Computerized Tomographic Imaging* (Institute of Electrical and Electronics Engineers, New York, 1988).
7. M. A. Franceschini, V. Toronov, M. E. Filiaci, E. Gratton, and S. Fantini, "On-line optical imaging of the human brain with 160-ms temporal resolution," Opt. Exp. **6,** 49–57 (2000); http://www.opticsexpress.org.
8. A. H. Hielscher, A. Y. Bluestone, C. H. Schmitz, R. L. Barbour, and G. S. Abdoulaev, "Volumetric imaging of hemodynamic effects in the human brain by three-dimensional diffuse optical tomography," in *Digest of Advances in Optical Imaging and Photon Migration*, OSA Biomedical Topical Meetings (Optical Society of America, Washington, D.C., 2002), pp. 310–312.
9. J. P. Culver, T. Durduran, D. Furuya, C. Cheung, J. H. Greenberg, and A. G. Yodh, "Diffuse optical measurement of hemoglobin and cerebral blood flow in rat brain during hypercapnia, hypoxia and cardiac arrest," Adv. Exp. Med. Biol. (to be published).
10. B. Chance, "Near-infrared (NIR) optical spectroscopy characterizes breast tissue hormonal and age status," Acad. Radiol. **8,** 209–210 (2001).
11. A. E. Cerussi, A. J. Berger, F. Bevilacqua, N. Shah, D. Jakubowski, J. Butler, R. Holcombe, and B. Tromberg, "Sources of absorption and scattering contrast for near-infrared optical mammography," Acad. Radiol. **8,** 211–218 (2001).
12. R. J. Gaudette, D. A. Boas, D. H. Brooks, C. A. DiMarzio, M. E. Kilmer, and E. L. Miller, "Comparison of linear reconstruction techniques for 3D DPDW imaging of absorption coefficient," in *Optical Tomography and Spectroscopy of Tissue III*, B. Chance, R. R. Alfano, and B. J. Tromberg, eds., Proc. SPIE **3597,** 55–66 (1999).
13. R. L. Barbour, H. L. Graber, Y. Pei, S. Zhong, and C. H. Schmitz, "Optical tomographic imaging of dynamic features of dense-scattering media," J. Opt. Soc. Am. A **18,** 3018–3036 (2001).
14. D. A. Boas, T. J. Gaudette, and S. R. Arridge, "Simultaneous imaging and optode calibration with diffusive optical tomography," Opt. Exp. **8,** 263–270 (2001); http://www.opticsexpress.org.
15. B. W. Pogue and M. S. Patterson, "Frequency-domain optical absorption spectroscopy of finite tissue volumes using diffusion theory," Phys. Med. Biol. **39,** 1157–1180 (1994).
16. M. S. Patterson, B. Chance, and B. C. Wilson, "Time-resolved reflectance and transmittance for the noninvasive measurement of tissue optical properties," Appl. Opt. **28,** 2331–2336 (1989).
17. B. J. Tromberg, L. O. Svaasand, T.-T. Tsay, and R. C. Haskell, "Properties of photon density waves in multiple-scattering media," Appl. Opt. **32,** 607–616 (1993).
18. M. A. O'Leary, D. A. Boas, B. Chance, and A. G. Yodh, "Refraction of diffuse photon density waves," Phys. Rev. Lett. **69,** 2658–2661 (1992).
19. S. R. Arridge, M. Schweiger, M. Hiraoka, and D. T. Delpy, "A finite element approach for modeling photon transport in tissue," Med. Phys. **20,** 299–309 (1993).
20. G. H. Golub and J. M. Ortega, *Scientific Computing and Differential Equations: An Introduction to Numerical Methods*, 2nd ed. (Academic, San Diego, Calif., 1981).
21. S. R. Arridge, "Optical tomography in medical imaging," Inverse Probl. **15,** R41–R93 (1999).
22. M. Born and E. Wolf, *Principles of Optics*, 7th ed. (Cambridge U. Press, New York, 1999).